ADVANCED FUNCTIONAL MATERIALS
www.afm-journal.de

www.MaterialsViews.com

Structural Determination and Imaging of Charge Ordering and Oxygen Vacancies of the Multifunctional Oxides $REBaMn_2O_{6-\chi}$ (RE = Gd, Tb)

*David Ávila-Brande, Graham King, Esteban Urones-Garrote, Subakti, Anna Llobet, and Susana García-Martín**

Charge ordering and oxygen vacancy ordering are revealed in $REBaMn_2O_{6-\delta}$ (RE = Gd, Tb) oxides with perovskite-related structures. Electron diffraction and transmission electron microscopy results indicate a modulation of the crystal structure. The average oxidation state of Mn and the oxygen stoichiometry are determined by means of electron energy-loss spectroscopy, giving a $REBaMn_2O_{5.75}$ general formula. A 1:3 Mn^{4+}:Mn^{3+} charge ordering model is confirmed by neutron powder diffraction, and oxygen vacancies-Mn^{3+} association is suggested by pair distribution function analysis. Direct imaging of the oxygen sublattice is obtained by phase image reconstruction. Location of the oxygen vacancies in the anion sublattice is achieved by analysis of the intensity of the averaged phase image. Both ionic conduction and multiferroic behavior are predicted from the crystal structures of these oxides.

1. Introduction

Transition metal (TM) oxides with perovskite-type structures exhibit a great variety of electronic and magnetic properties. The so-called manganites are among those 3d-TM perovskites with strong correlation of partially localized electrons that originate a close interplay of spin, charge, orbital, and lattice degrees of freedom, and are responsible for important properties such as colossal magnetoresistance or metal–insulator transitions accompanied by the charge and orbital order.

Ordering/disordering phenomena of the cations can also produce significant variations on the correlation/competition of degrees of freedom with important impact on the properties of these oxides. In this sense, ordering/disordering effects on the electronic properties of $REBaMn_2O_6$/$RE_{0.5}Ba_{0.5}MnO_3$ perovskites have been widely reported.[1–6] In the $REBaMn_2O_6$ oxides, the RE^{3+} and Ba^{2+} cations are ordered in alternating [001] perovskite planes; this is the layered-type ordering.[7] The electronic phase diagram of the *A*-site ordered $REBaMn_2O_6$ establishes different groups of compounds depending on the RE ion size:[3–6] the ground states of the La, Pr, and Nd manganites are ferromagnetic metals (FM) while the oxides with RE cations smaller than Nd show a charge orbital ordering insulator state (COOI). On the contrary, the disordered $RE_{0.5}Ba_{0.5}MnO_3$ manganites with RE cations smaller than Nd show paramagnetic behavior.

Charge order (CO) structures have been experimentally evidenced by several techniques in $REBaMn_2O_6$ perovskites and different CO models have been proposed from powder neutron diffraction, electron diffraction and resonant X-ray and Raman scattering experiments.[8–13] Of particular interest is that multiferroic properties have been ascribed to some manganites [14,15] due to coupling between magnetic and charge ordering.

In addition to these multiple ordering effects, a certain range of non-stoichiometry within the anion sublattice is often found in manganites, which is also responsible for interesting electronic properties.[7] In this case, mixed-conductivity can occur due to the oxygen anions moving throughout the anion vacancies. Moreover, in the layered-type ordered $REBaMn_2O_{6-\delta}$ the anion vacancies are expected to be mainly located close to the rare earth atoms forming very high conducting planes, which increase the oxygen-ion diffusion in comparison with the *A*-cation-disordered perovskites,[16,17] and making these compounds promising candidates as cathodes in solid oxide fuel cells. The atomic mechanism of diffusion can be understood by knowing the vacancy distribution within the oxygen sublattice.

Certain instrumental improvements in high resolution transmission electron microscopy (HRTEM) such as reduction of spherical and chromatic aberration of the electron-optical lens system and techniques like scanning-TEM (STEM) have proven to give a new insight into atomic resolution structure determination. However, only digital exit surface wave reconstruction processing of focal image series provides information on quantification of vacancies within an atomic column of oxygen atoms. The benefit of using this technique in combination with

Dr. D. Ávila-Brande, Subakti, Dr. S. García-Martín
Departamento de Química Inorgánica
Universidad Complutense de Madrid
Madrid, 28040, Spain
E-mail: sgmartin@quim.ucm.es
Dr. G. King, Dr. A. Llobet
Lujan Neutron Scattering Center
Los Alamos National Laboratory
Los Alamos, NM, 87545, USA
Dr. E. Urones-Garrote
Centro,Nacional de Microscopía Electrónica
Universidad, Complutense de Madrid
Madrid, 28040, Spain

DOI: 10.1002/adfm.201303564

the hardware correction of the spherical aberration is to achieve directly from the images a better resolution limit rather than the point resolution of the microscope.[18] This allows for the identification of the light oxygen atoms in the phase image of the exit wave and by means of structure modeling and quantum-mechanical simulations of the electron scattering process to quantify the oxygen occupancy column by column. In this context, exit wave reconstruction (EWR) has been used to reveal oxygen concentration in the twin boundaries of $BaTiO_3$ films[19] and nonstoichiometry and distortion of the oxygen octahedra sublattice at the dislocations of $SrTiO_3$.[20] Apart from these microscopy techniques, neutron diffraction experiments give extraordinary information of different arrangements associated to the anion-sublattice of oxides. In this sense, average anion vacancy ordering and other ordering effects leading to anion displacements, such as charge ordering, can be determined by Rietveld refinement of neutron diffraction data. In combination to Rietveld refinement, pair distribution function (PDF) analysis provides complementary information on the local structure and disorder by giving the distributions of inter-atomic distances in the structure.

We report in this article the crystal structures of $GdBaMn_2O_{6-\delta}$ and $TbBaMn_2O_{6-\delta}$ studied by a combination of techniques: selected area electron diffraction (SAED), HRTEM, electron energy loss spectroscopy, powder neutron diffraction, PDF analysis, and EWR image processing. The different techniques used in this work have provided complementary information that has allowed us to propose a new model of charge ordering and anion vacancies ordering in these manganites. Interesting properties of these compounds like multiferroic behavior and ionic conductivity can be derived from the following described ordering effects.

2. Results and Discussion

The XRD patterns of the compounds show superlattice reflections of the perovskite structure, suggesting a lowering of the symmetry and ordering of the Ba and Gd/Tb atoms (the $½(001)_p$ reflection appears, which is associated to layered-type ordering of the cations; *p* refers to the cubic perovskite subcell).

A study of the reciprocal lattice has been performed by taking SAED patterns along different zone axis of crystals of $GdBaMn_2O_{6-\delta}$ and $TbBaMn_2O_{6-\delta}$. Both compounds show similar results. **Figure 1**a–c shows SAED patterns along three different zone axis of a crystal of $GdBaMn_2O_{6-\delta}$. In addition to the Bragg reflections of the perovskite structure, there are strong superlattice reflections at $G_p \pm ½(001)^*_p$ and weak superlattice reflections at $G_p \pm 1/4(110)^*_p$, $G_p \pm 1/2(-111)^*_p$ and $G_p \pm 1/4(-221)^*_p$, which suggest a modulation of the crystal structure along the $[110]_p$ and $[001]_p$ directions. The $½(001)_p$ reflection also appears in the XRD patterns and is associated with layered-type ordering of the Ba and Gd/Tb cations. On the contrary, the weak reflections along the $[110]_p$ and $[001]_p$ directions are not distinguished in the XRD patterns of these compounds. The unit cell of the modulated structure deduced from the reciprocal lattice constructed from different SAED patterns is $\sqrt{2}a_p \times 2\sqrt{2}a_p \times 4a_p$. Tilting of the reciprocal lattice indicates that the weak (0*k*0) reflections with $k = 2n+1$ in the new unit cell are due to multiple diffraction. Therefore, the reflection conditions deduced from the SAED patterns ((00*l*) reflections with $l = 2n$ and (0*k*0) reflections with $k = 2n$) point to space group $P22_12_1$, #18 ($P2_12_12$ in the standard setting). Figure 1d,e shows two HRTEM images and the corresponding SAED patterns of a crystal of $GdBaMn_2O_{6-\delta}$ along the $[001]_p$ and $[-1-10]_p$ zone axes. Contrast differences indicating a four-fold superstructure along the $[110]_p$ direction are clearly seen. On the contrary, $4a_p$ periodicity is not observed in the image of the $[-1-10]_p$ zone axis, despite it is concluded from the corresponding FFT and the SAED patterns; only $2a_p$ periodicity is distinguished. This fact indicates that the effect creating the $2a_p$ periodicity produces contrast differences in the images significantly stronger that the effect associated with the $4a_p$ periodicity or the fourfold superstructure along the $[001]_p$ direction.

In order to evaluate the oxidation state of Mn and therefore the oxygen stoichiometry, EELS experiments have been carried out. The energy-loss near-edge structures (ELNES) of L-ionization edges of the transition metals in oxides show characteristic white lines due to transitions of excited 2p core electrons into unoccupied d-orbitals.[21] The quantitative analysis of those absorption edges give direct information about the transition metal oxidation state. The measurement of the white-line intensity ratio (L_3/L_2) is one of the established methods to extract this data.[22] Following the procedure reported by Schmid and Mader,[23] we built up a curve

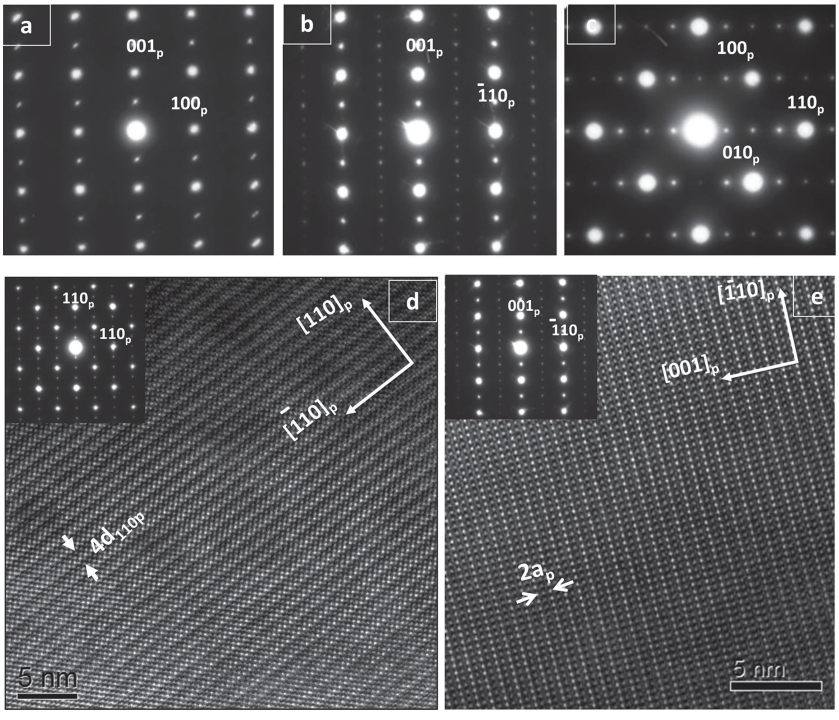

Figure 1. SAED patterns of a $GdBaMn_2O_{6-\delta}$ crystal along the a) $[010]_p$, b) $[-1-10]_p$, and c) $[001]_p$ zone axes. HRTEM images of a $GdBaMn_2O_{6-\delta}$ crystal recorded along d) the $[001]_p$ and e) the $[-1-10]_p$ zone axes.

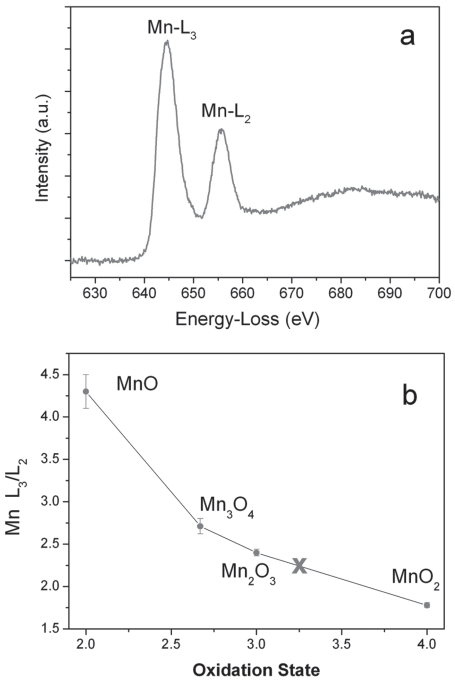

Figure 2. a) Typical Mn-$L_{2,3}$ ionization edge of a $GdBaMn_2O_{6-\delta}$ crystal; b) Graphic representation of L_3/L_2 intensity ratio versus Mn oxidation state in standard Mn oxides and in the studied sample (cross).

relating oxidation state and L_3/L_2 intensity ratio (see **Figure 2**b), employing four Mn oxides as standards. The L_3/L_2 intensity ratio of the $GdBaMn_2O_{6-\delta}$ sample (acquiring spectra from 10 different crystals, see a typical one in Figure 2a) corresponds to an average oxidation state for Mn of 3.24 ± 0.06 (crossing in Figure 2b); similar results were found for $TbBaMn_2O_{6-\delta}$. This value suggests the presence of one Mn^{4+} and three Mn^{3+} per general formula and an oxygen stoichiometry around 5.75, taking into account that the composition of the cation sublattice is deduced from XEDS data.

Therefore, the SAED and HRTEM results indicate that $GdBaMn_2O_{5.75}$ and $TbBaMn_2O_{5.75}$ show a modulated perovskite-type structure with a $\sqrt{2}a_p \times 2\sqrt{2}a_p \times 4a_p$ unit cell. Layered-type ordering of Ba and Gd is evidenced from the XRD and SAED patterns and also from HRTEM results. This type of ordering leads to a two-fold superstructure of the perovskite: superlattice reflections at $G_p \pm \frac{1}{2}(001)^*_p$ and the strong contrast differences giving a $2a_p$ periodicity along $[001]_p$ direction. In addition to the cation ordering, a modulation of the crystal structure along $[110]_p$ and $[001]_p$ directions is detected by the existence of superlattice reflections at $G_p \pm 1/4(110)^*_p$, $G_p \pm 1/2(-111)^*_p$, and $G_p \pm 1/4(-221)^*_p$ and the contrast differences in the HRTEM images of the $[-1-10]_p$ zone axis. This modulation of the crystal structure must be associated to a new type of effect such as anion vacancies ordering, charge ordering, or both. In this sense, charge ordering at room temperature is predicted in $REBaMn_2O_6$ oxides with RE ions of smaller size than Nd.[4,5] Other $REBaMn_2O_6$ manganites, such as $SmBaMn_2O_6$ and $TbBaMn_2O_6$ have been studied by SAED [8,9] and $YBaMn_2O_6$ by SAED and HRTEM.[10] All of them show SAED patterns similar to those in Figure 1 and CO was ascribed to the modulation of their crystal structure. Several models for the CO structure of these manganites have been proposed so far.[8–13] However, all of these models are based on stoichiometric oxides (equal amount of Mn^{3+} and Mn^{4+}), which is not the case of our compounds. According to our EELS results, the average oxidation state of the Mn is 3.24 ± 0.06, which corresponds to 1 Mn^{4+} and 3 Mn^{3+} for general formula and non-stoichiometry in the anion sublattice ($REBaMn_2O_{5.75}$). Therefore, we have to propose a new model of CO which agrees with the $REBaMn_2O_{5.75}$ composition and the $\sqrt{2}a_p \times 2\sqrt{2}a_p \times 4a_p$ unit cell.

CO phenomena is also ascribed to the low temperature modulation of the crystal structure in $La_{1-x}Ca_xMnO_3$[24] and $Sm_{1-x}Ca_xMnO_3$.[25,26] Different models of ordering of Mn^{3+} and Mn^{4+} stripes along the $[110]_p$ direction are proposed for the different x values in these manganites. Commensurate ordering is observed for rational x values: one Mn^{3+} stripe alternates with two Mn^{4+} stripes for $x = 2/3$ and one Mn^{3+} stripe alternates with three Mn^{4+} stripes for $x = 3/4$. An incommensurate ordering is observed for irrational x values. CO at room temperature is evidence as well in $Bi_{1-x}Sr_xMnO_3$ by SAED and HRTEM.[27,28] In these Bi-manganites, models built up of double Mn^{3+} stripes alternating with double or quadruple Mn^{4+} stripes are suggested for $x = 1/2$ and $x = 1/3$ respectively.

Based on these previous results and taking into account that our compounds have around 75% of Mn^{3+} and 25% of Mn^{4+}, we propose a CO model which consists of one Mn^{4+} stripe alternating with three Mn^{3+} stripes along the $[110]_p$ direction (**Figure 3**a). This CO originates a $\sqrt{2}a_p \times 2\sqrt{2}a_p$ periodicity, in

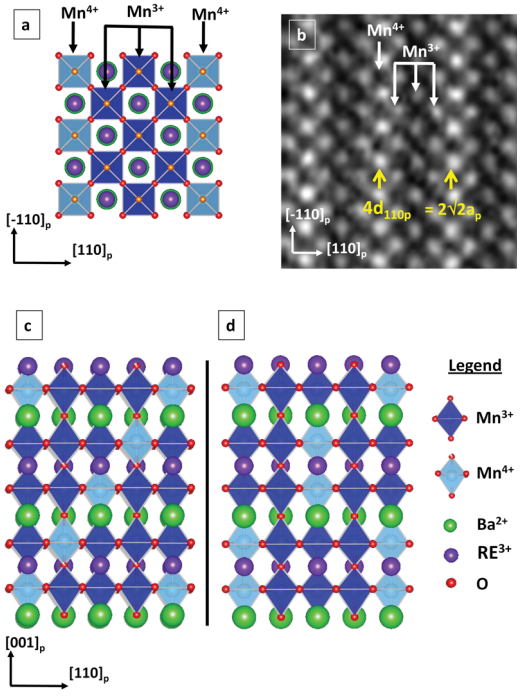

Figure 3. a) Schematic representation of the 1:3 Mn^{4+}:Mn^{3+} ordering within the $(001)_p$ plane. b) Enlargement from Figure 1d where the contrast differences suggest the charge ordering represented in (a). c,d) Ideal structural models proposed for the stacking of the layers along *c*.

agreement with the ED analysis and the differences in contrast observed in HRTEM (Figure 3b).

Packing of these layers along the *c*-direction, leading to a $4a_p$ periodicity, has to be considered for constructing the 3D CO structure. There are different kinds of packing giving a $4a_p$ periodicity along *c*, like for instance those indicated in Figure 3c,d, but the strong contrast differences in the HRTEM images of the $[-1-10]_p$ zone axis due to Ba/Gd ordering ($2a_p$) periodicity does not allow to distinguished contrast differences associated to the $4a_p$ periodicity. Therefore, we have tried to solve the crystal structure of these compounds by powder neutron diffraction for $TbBaMn_2O_{5.75}$.

Charge ordering in oxides can often be identified by small shifts in oxygen atom positions which are due to the different bond lengths the oxygen makes with cations of different oxidation states. Neutron powder diffraction (NPD) is an ideal probe for investigating the subtle superstructures that result from charge ordering since, unlike XRD, it has a high sensitivity to oxygen atom positions. Due to the very high neutron absorption cross section of Gd this technique could only be used to study the $TbBaMn_2O_{5.75}$ sample. An NPD pattern of $TbBaMn_2O_{5.75}$ was collected at 300 K. All of the major peaks in the NPD pattern could be indexed using a simple $a_p \times a_p \times 2a_p$ unit cell with space group *P*4/*mmm*. The *P*4/*mmm* structural model represents the aristotype structure for *A*-site layered oxygen deficient perovskites.[7] In this model there is a layered ordering of Tb and Ba along the $[001]_p$ direction and the oxygen vacancies are randomly distributed exclusively within the Tb layer.

There is only a single site for Mn in this model so it cannot accommodate charge ordering. Rietveld refinements using this model have been able to provide a fairly good fit to the peak intensities (**Figures 4**a and Supporting Information Figure S1). The refinements gave subcell parameters of a = 3.9025(2) Å and c = 7.5925(3) Å. Moreover, oxygen occupancies have been refined verifying the overall oxygen content determined by EELS. There are about 16 very weak additional peaks evident in the NPD pattern that are not indexed by this unit cell (see inset in Figure 4a). The positions of these peaks were checked against the expected peak positions of likely impurity phases but none of the peaks could be attributed to any secondary phases. These weak additional peaks have all been indexed using the $\sqrt{2}a_p \times 2\sqrt{2}a_p \times 4a_p$ unit cell determined by SAED. The fact that the simple *P*4/*mmm* model is able to index all peaks except for some very weak ones and provide a reasonably good fit to the intensities of all major peaks shows that the superstructure which results from charge ordering involves only subtle displacements of atoms from their ideal positions. Also, while the SAED and HRTEM results show that the symmetry is no higher than orthorhombic, the good fit obtained using the *P*4/*mmm* model shows that the sub-cell metrics must be highly pseudo-tetragonal.

The $\sqrt{2}a_p \times 2\sqrt{2}a_p$ periodicity within the *ab*-plane can be attributed to a 1:3 Mn^{4+}:Mn^{3+} striped ordering as shown in Figure 3. There are two simple ways in which layers of these stripes could stack in order to produce a $4a_p$ periodicity along the *c*-axis. These are shown in Figures 3c and d. One way would be for the CO layers to shift by $1a_p$ along the $[100]_p$ direction every layer along *c* (Figure 3c).

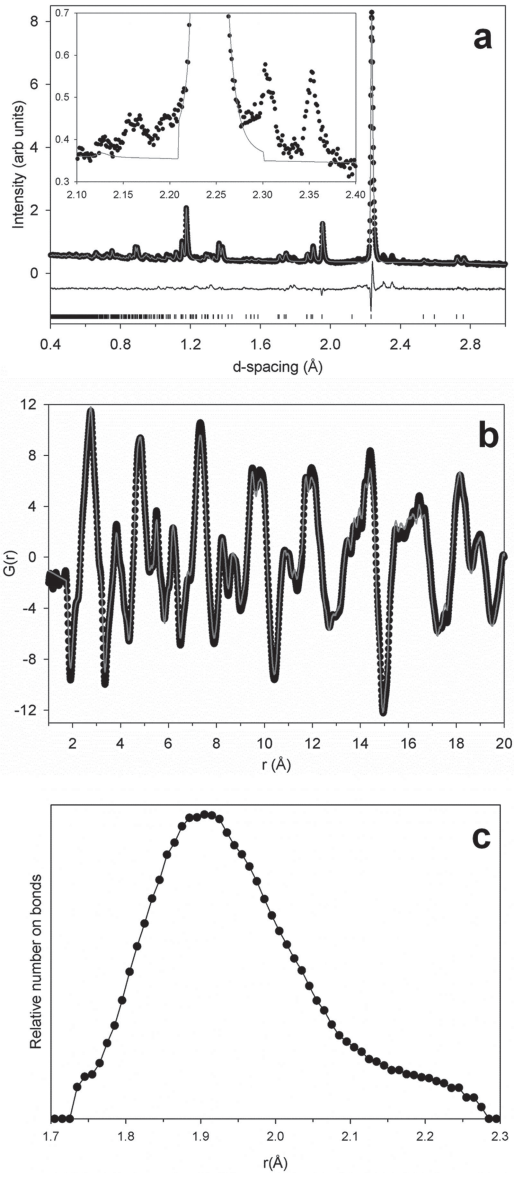

Figure 4. a) NPD pattern of $TbBaMn_2O_{5.75}$ collected on the 153° backscattering bank of HIPD (black circles), the fit using the *P*4/*mmm* aristotype model (red), and the difference (beneath). The tick marks show the allowed *hkl* positions for the aristotype structure. The inset shows some of the weak unfit reflections. b) RMC fit to the PDF. Black dots are experimental data points and the red line is the fit. c) Distribution of Mn–O bond lengths extracted from the RMC configuration. The low number of long bonds and the lack of a low-r should indicate that the O vacancies are concentrated between pairs of Mn^{3+} and that all Mn^{4+} are 6 coordinate.

The other way would be to have CO bilayers which are shifted by $2a_p$ along the $[100]_p$ direction every other layer along *c* (Figure 3d). In order to determine which of these two possibilities is responsible for the $4a_p$ periodicity in these compounds $P22_12_1$ space group symmetry, deduced from the construction of the reciprocal lattice from the SAED patterns, has been imposed on $\sqrt{2}a_p \times 2\sqrt{2}a_p \times 4a_p$ expansion of the aristotype structure. By examining how the symmetrically unique

Mn atoms where arranged it was apparent that the unique Mn atoms were arranged into bilayers. An idealized representation of this kind of structure is shown in Figure 3d. It is important to note that $P22_12_1$ is a polar space group and therefore the charge ordering observed in $TbBaMn_2O_{5.75}$ can lead to ferroelectricity. Furthermore, since the charge ordering will directly affect the magnetic ordering strong magnetoelectric coupling can also be expected, making these materials promising candidates for strongly coupled multiferroic materials.

Rietveld refinements were attempted using the $P22_12_1$ structure as a starting model. These refinements were not stable and therefore precise atomic positions could not be determined. There are a large number of structural degrees of freedom in this model and since the superstructure results in only a few additional weak peaks in the NPD pattern, the number of peaks is insufficient to consistently refine the number of variables in this model without imposing constrains. While the structure could not be fully solved by Rietveld analysis, additional information on the oxygen vacancy distribution and the bond lengths was obtained by PDF analysis.

The PDF gives the radial distribution of inter-atomic distances for all atom-atom pairs in the material. By modeling the PDF, the distribution of inter-atomic distances for specific pairs of atoms can be extracted. By looking at the distribution of Mn–O bond distances in $TbBaMn_2O_{5.75}$ information on the oxidation states of the Mn cations and the positions of the oxygen vacancies within the TbO layer can be obtained. The PDF of $TbBaMn_2O_{5.75}$ was modeled using the "large box" Reverse Monte Carlo (RMC) method. A $12 \times 12 \times 8$ supercell of the $P4/mmm$ subcell containing 11 230 atoms and 290 vacancy positions was created to model the data. The positions of the atoms in this supercell were adjusted to fit the experimental $G(r)$ and $S(Q)$ functions. The final fit to the data is shown in Figure 4b. The inter-atomic distances for all atom-atom pairs are given in Supporting Information Figure S2. The Mn–O bond distance distribution is shown in Figure 4c.

The coordination numbers of the Mn^{4+} and Mn^{3+} cations can be determined from their bond lengths. The Mn^{4+} cation tends to have a symmetric coordination environment with bond lengths around 1.90 Å when six coordinate and 1.84 Å when 5 coordinate. The Mn^{3+} cation is susceptible to a first order Jahn-Teller distortion and tends to have an asymmetric coordination. When it is six coordinate it tends to have four short bonds in the range of 1.90–1.97 Å and two long bonds around 2.15–2.23 Å. When only 5 coordinate it also has four short bonds but now only one long bond which is shortened to only 2.05–2.10 Å. The Mn–O bond distribution obtained from the RMC fitting peaks at 1.91 Å and gives an average Mn–O distance of 1.94 Å. The distribution is highly asymmetric, falling off sharply on the low-r side of the peak but having a shoulder on the high-r side from long Mn^{3+}–O bonds. If the oxygen vacancies were randomly distributed then 19.6% of all Mn–O bonds should be long bonds around 2.2 Å and there should be some bonds below 1.90 Å from 5 coordinate Mn^{4+}.

If the vacancies only occurred between Mn^{3+} cations, then the distribution could be expected to be narrower, with no very short bonds and fewer very long bonds. The lack of a shoulder in the Mn–O distribution at 1.84 Å and the fact that the number of very long Mn–O bonds appears to be less than expected from a random distribution indicates that all of the Mn^{4+} are 6 coordinate and the O vacancies are all concentrated between pairs of Mn^{3+} cations resulting in more 5 coordinate Mn^{3+} than if the O vacancies were random. This shows that there is at least some degree of oxygen vacancy ordering within the TbO layers. **Figure 5** shows two different orientations of the crystal structure of the compounds.

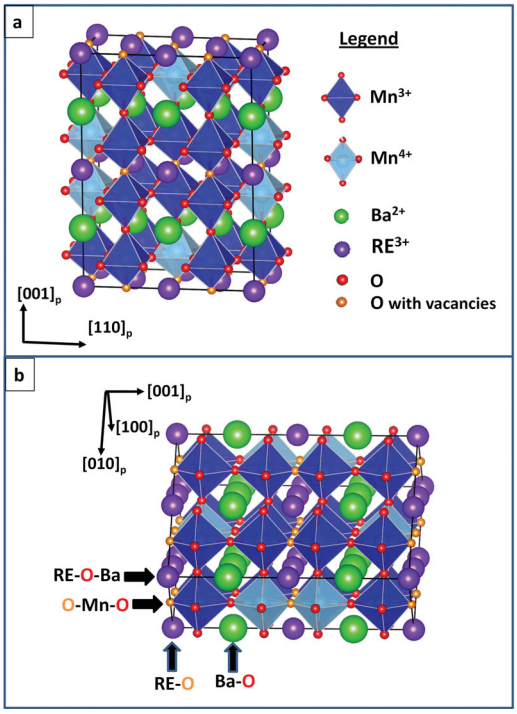

Figure 5. a) Crystal structure model determined for $REBaMn_2O_{5.75}$. b) Crystal orientation showing isolated oxygen atomic columns containing vacancies (in orange) within the RE-O layers and ordered with fully occupied oxygen columns (in red) through the $[001]_p$ direction.

To probe the validity of the structural model determined from Rietveld refinement of neutron diffraction data and PDF analysis and to get direct information of the preferred location of the oxygen vacancies, we have performed an exit wave reconstruction (EWR) experiment. By selecting the appropriate structure projection, we can directly observe if the oxygen vacancies are located in those positions suggested by our PDF results.

The analysis of the structural model deduced from the NPD and PDF results indicates that the different atomic columns are clearly distinguishable in its projection along the $[010]_p$ zone axis(see Figure 5). The Mn atomic columns are sandwiched in an ordered way (Mn^{3+} and Mn^{4+}) by pure atomic columns of RE and Ba layers along the $[001]_p$ direction. Besides, the oxygen sublattice shows an ordering of the vacancies along both $[100]_p$ and $[001]_p$ due to their location at the RE planes and coordinated to the Mn^{3+} atoms. Only along this projection of the structure columns of RE atoms are isolated from columns of Ba atoms. Other projections give columns of RE atoms alternating with Ba atoms. On the contrary, there is not any projection of the structure which allows isolation of columns of Mn^{3+} atoms and columns of Mn^{4+} atoms (i.e., the two types of Mn atoms cannot be distinguished in the images). Therefore, by

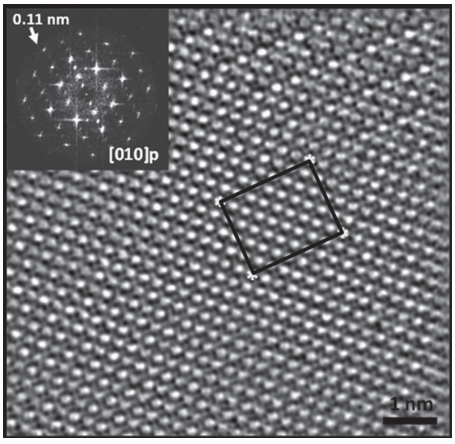

Figure 6. Reconstructed phase image of the exit wave along $[010]_p$. The IFFT on the upper left shows the information limit reached after the exit wave reconstruction.

EWR processing we are able to locate the anion vacancies only in the RE planes but unfortunately we will not obtain information of the vacancies-Mn^{3+} coordination.

A focal series of 20 images with an equidistant focal decrease has been recorded along the $[010]_p$ zone axis using a slow-scan CCD camera. The reconstruction and numerical correction for the aberrations have been performed using the IWFR. The reconstructed phase image is presented in **Figure 6**, where the positions of the different type of atomic columns appear as bright dots. It is very important to note that the light oxygen atoms are also imaged as fainter white dots.

In order to further improve the signal-to-noise ratio, we have used a custom written algorithm implemented in the iMtools package to average the phase of the reconstructed exit-plane wave function. The average has been performed in the region marked by yellow asterisk on the phase image (Figure 6 and Supporting Information Figure S3), and the corresponding region has been replaced by the averaged resulting image showing a clear improvement of the signal to noise ratio (Figure 6 and Figure S3 in the Supporting Information). The inset to the upper left of the phase image shows the fast Fourier transform, where we observe that the limit resolution of the microscope 0.11 nm is reached.

A closer analysis of the intensity of averaged phase image was performed in the magnified area displayed in **Figure 7**a. Since the phase of the exit wave is proportional to the projected electrostatic potential of the structure, the careful analysis of the intensity of the different columns along the image allows us to identify and overlay the position of the different atom columns (green symbols denote Ba columns, purple RE, blue Mn, red O1 columns of O atoms, and orange O2 columns of O atoms and vacancies). In addition to this, the simulated phase image for the appropriate structure and microscope settings has been superimposed the experimental one at the bottom, showing the same features.

The intensity profile along the $[001]_p$ direction of the row marked by green arrows in Figure 7a clearly reproduces the ordering of RE and Ba along [001]p with the intensity maxima

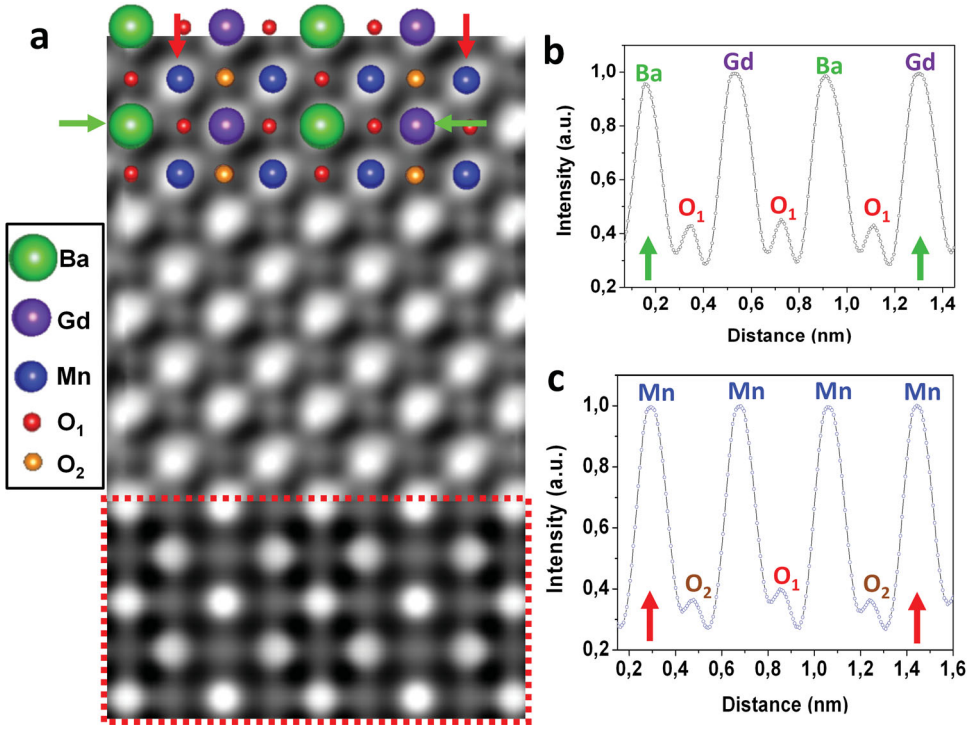

Figure 7. a) Enlargement of the averaged phase image marked by yellow asterisks in Figure 6; the bright dots correspond to the projected potential of the different atomic columns identified by the colors represented in the legend, at the bottom the calculated phase image (thickness = 3.12 nm) is displayed showing good correspondence. b,c) Intensity profiles performed along the directions marked by green and red arrows respectively in (a).

belonging to the RE slightly higher, and with the oxygen peaks showing a similar intensity (Figure 7b). More interesting is the profile (shown in Figure 7c) of the row of Mn–O columns marked by red arrows in Figure 7a running along the $[100]_p$ direction.

Here, the peaks with higher intensity correspond to the Mn columns, whereas the peaks belonging to the O columns exhibit a weaker intensity and vary regularly, with lower intensity in those columns located near the RE atomic columns and higher when the closest atom is Ba. This situation agrees, with the fact that O vacancies will preferentially lie within the RE layer, in agreement with the NPD analysis.

3. Conclusions

A combination of techniques has allowed us to solve the crystal structure of $GdBaMn_2O_{5.75}$ and $TbBaMn_2O_{5.75}$. The structures are related to the perovskite-type with a superlattice due to charge and anion vacancies ordering which is present at room temperature. Layered-type ordering of the Ba and RE cations may drive this complex association between CO and the location of the anion vacancies within the RE planes. SAED and HRTEM have revealed the modulation of the structure with unit cell $\sqrt{2}a_p \times 2\sqrt{2}a_p \times 4a_p$ and by EELS experiments we have quantified the average oxidation state of Mn and therefore the anion stoichiometry of the compounds. We have suggested, in addition to the layered ordering of the Ba/RE cations, a CO model within the $(001)_p$ planes, which accounts for one Mn^{4+} stripe alternating with three Mn^{3+} stripes along the $[110]_p$ direction. By NPD we have confirmed the CO model, determined the 3D packing of the $(001)_p$ planes, which consists of CO bilayers shifted by $2a_p$ along the $[100]_p$ direction every other layer along $[001]_p$ and have located the anion vacancies within the RE planes. PDF analysis also has revealed coordination of the Mn^{3+} cations to the anion vacancies. This crystal structure model, determined from NPD, has been used to perform EWR experiments, reconstructing a phase image along the $[010]_p$ zone axis which clearly shows imaging of the oxygen sublattice at the unit cell level. Analysis of the intensity of the averaged phase image has revealed columns with lower occupation of oxygen atoms, which has allowed us to locate the anion vacancies within the RE planes of the structure. $GdBaMn_2O_{5.75}$ and $TbBaMn_2O_{5.75}$ might have interesting properties such as oxygen conduction or multiferroic behavior that could be explained taking into account their crystal structure and particularly the combination of the ordering effects in the structure.

4. Experimental Section

Synthesis: Polycrystalline samples of $GdBaMn_2O_{6-\delta}$ and $TbBaMn_2O_{6-\delta}$ have been prepared from stoichiometric amounts of $BaCO_3$, Mn_2O_3, and Gd_2O_3 or Tb_4O_7. Gd_2O_3 and Tb_4O_7 were dried overnight at 1000 °C prior to being weighed. The mixtures were ground and heated in Ar flow, initially at 1000 °C during 4 h for decarbonation. Afterwards, the samples were ground, pelleted, and fired at 1300 °C for 24 h in Ar followed by a further grinding, pelleting, and firing at 500 °C for another 12 h in O_2 flow to complete the reaction.

Characterization: Crystalline phase identification was carried out by powder X-ray diffraction (XRD) using a Philips X'PERT diffractometer with Cu Kα1 radiation (λ = 1.5406 Å) and with a curved Cu monochromator. The atomic ratio of the metals was determined by X-ray energy dispersive spectroscopy (XEDS) analyses finding good agreement between analytical and nominal composition. For transmission electron microscopy the samples were ground in *n*-butyl alcohol and ultrasonically dispersed. A few drops of the resulting suspension were deposited in a carbon-coated grid. SAED and HRTEM studies were carried out with a JEM 3000F microscope operating at 300 kV (double tilt (±20°) (point resolution 1.7 Å), fitted with a XEDS microanalysis system (OXFORD INCA). Electron Energy-Loss Spectroscopy (EELS) experiments were performed in a Philips CM200FEG microscope, fitted with a GIF 200 (energy resolution ≈ 0.8 eV). The spectra were acquired in diffraction mode, with a dispersion of 0.1 eV px^{-1}, a collection angle β = 3.3 mrad and an acquisition time of 2 s. The background of all the raw spectra was removed using a power-law model. When necessary, plural-scattering effects were removed with a Fourier-ratio deconvolution method. Focus series of twenty images were recorded with a focal increment of 3 nm starting from –144 nm. The exit-plane wave was reconstructed and residual aberrations were numerically corrected for the complex valued exit-plane wave using the IWFR software,[29] reaching the information limit of the JEM 3000F microscope (0.11 nm). The phase image was digitally processed with iMTools electron microscope processing software[30] and exit-plane wave function was simulated for reference using MacTempas X.[31]

Time-of-flight neutron powder diffraction data was collected for the $TbBaMn_2O_{6-\delta}$ sample on the HIPD instrument at the Lujan Center of Los Alamos National Laboratory. The Rietveld refinements were done using the GSAS/EXPGUI software.[32,33] The pair distribution function, $G(r)$, was generated from the neutron total scattering data using the PDFgetN program using a Q_{max} of 31 $Å^{-1}$.[34] Reverse Monte Carlo modeling of the $G(r)$ was done using the program RMCProfile.[35]

Supporting Information

Supporting Information is available from the Wiley Online Library or from the author.

Acknowledgements

S.G.-M., D.A.-B., S. and E.U.-G. thank the Spanish MEC for funding Projects MAT2010–19837-C06–03, MAT2010–19460 and PIB2010JP-00181; CAM for Project MATERYENER-2 P2009/PPQ-1629 and EC for SOPRANO. FP7-PEOPLE-2007–1–1-ITN. This work has benefited from the use of HIPD at the Lujan Center at Los Alamos Neutron Science Center, funded by DOE Office of Basic Energy Sciences. Los Alamos National Laboratory is operated by Los Alamos National Security LLC under DOE Contract DE-AC52–06NA25396.

Received: October 18, 2013
Published online: December 27, 2013

[1] F. Millange, V. Caignaert, B. Domengès, B. Raveau, *Chem. Mater.* **1998**, *10*, 1974.
[2] S. V. Trukhanov, I. O. Troyanchuk, M. Hervieu, H. Szymczak, K. Bärner, *Phys. Rev. B.* **2002**, *66*, 184424.
[3] T. Nakajima, H. Kageyama, H. Yoshizawa, Y. Ueda, *J. Phys. Soc. Japan* **2002**, *71*, 2843.
[4] Y. Ueda, T. Nakajima, *J. Phys. Condens. Matter* **2004**, *16*, S573.
[5] T. Nakajima, H. Yoshizawa, Y. Ueda, *J. Phys. Soc. Japan* **2004**, *73*, 2283.

[6] T. Nakajima, H. Kageyama, H. Yoshizawa, K. Ohoyama, *J. Phys. Soc. Japan* **2003**, *72*, 3237.
[7] G. King, P. M. Woodward, *J. Mater. Chem.* **2010**, *20*, 5785.
[8] M. Uchida, D. Akahoshi, R. Kumai, Y. Tomioka, T. Arima, T. Tokura, Y. Matsui, *J. Phys. Soc. Japan* **2002**, *71*, 2605.
[9] T. Arima, D. Akahoshi, K. Oikawa, T. Kamirama, M. Uchida, Y. Matsui, T. Tokura, *Phys. Rev. B.* **2002**, *66*, 140408.
[10] H. Kageyama, T. Nakajima, M. Ichihara, Y. Ueda, H. Yoshizawa, K. Ohoyama, *J. Phys. Soc. Japan* **2003**, *72*, 241.
[11] A. J. Williams, J. P. Attfield, *Phys. Rev. B.* **2005**, *72*, 024436.
[12] A. J. Williams, J. P. Attfield, *Phys. Rev. B.* **2002**, *66*, 220405(R).
[13] D. Akahoshi, Y. Okimoto, M. Kubota, R. Kumai, T. Arima, Y. Tomioka, Y. Tokura, *Phys. Rev. B.* **2004**, *70*, 064418.
[14] D. V. Efremov, J. van den Brink, D. I. Khomskii, *Nat. Mater.* **2004**, *3*, 853.
[15] C. R. Serrao, A. Sundaresan, C. N. R. Rao, *J. Phys.: Condens. Matter* **2007**, *19*, 496217.
[16] A. A. Taskin, A. N. Lavrov, A. Yoichi, *Appl. Phys. Lett.* **2005**, *86*, 091910.
[17] A. A. Taskin, A. N. Lavrov, A. Yoichi, *Prog. Solid State Chem.* **2007**, *35*, 481.
[18] W. M. J. Coene, A. Thust, M. de Beeck, D. Van Dyck, *Ultramicroscopy* **1996**, *64*, 109.
[19] C. L. Jia, K. Urban, *Science* **2004**, *303*, 2001.
[20] C. L. Jia, A. Thust, K. Urban, *Phys. Rev. Lett.* **2005**, *95*, 225506.
[21] R. F. Egerton, *Electron Energy-Loss Spectroscopy in the Electron Microscope*, 3rd ed., Springer, New York, **2011**.
[22] H. Tan, J. Veerbeck, A. Abakumov, G. Van Tendeloo, *Ultramicroscopy* **2012**, *116* 24.
[23] H. K. Schmid, W. Mader, *Micron* **2006**, *37*, 426.
[24] C. H. Chen, S. W. Cheong, H. Y. Hwang, *J. Appl. Phys.* **1997**, *81*, 4326.
[25] M. Hervieu, A. Barnabé, C. Martin, A. Maignan, F. Damay, B. Raveau, *Eur. Phys. J. B* **1999**, *8*, 31.
[26] M. Hervieu, A. Barnabé, C. Martin, A. Maignan, F. Damay, B. Raveau, *J. Mater. Chem.* **1998**, *8*, 1405.
[27] M. Hervieu, A. Maignan, C. Martin, N. Nguyen, B. Raveau, *Chem. Mater.* **2001**, *13*, 1356.
[28] M. Hervieu, S. Malo, O. Perez, P. Beràn, C. Martin, G. Baldinozzi, B. Raveau, *Chem. Mater.* **2003**, *15*, 523.
[29] IWFR, version 1.0; HREM Research Inc.: Higashimastuyama, Japan, Feb **2005**.
[30] L. Houben, iMtools electron microscope image processing software, Research Center Jülich, http://www.er-c.org/methods/software.htm (accessed: 2013).
[31] Mac Tempas X. Version 2.3.7. A program for simulating HRTEM images and diffraction patterns.
[32] B. H. J. Toby, *Appl. Crystallogr.* **2001**, *34*, 210.
[33] A. C. Larson, R. B. Von Dreele, Los Alamos National Laboratory Report No. LAUR 86–748, **2004**.
[34] P. F. Peterson, M. Gutmann, Th. Proffen, S. J. L. Billinge, *J. Appl. Crystallogr.* **2000**, *33*, 1192.
[35] M. G. Tuker, D. A. Keen, M. T. Dove, A. L. Goodwin, Q. Hui, *J. Phys.: Condens. Matter* **2007**, *19*, 335218.